



Crystal chemistry and ionic conductivity of garnet-type solid-state electrolyte, $\text{Li}_{5-x}\text{La}_3(\text{NbTa})\text{O}_{12-y}$

Amrit P. Kafle ^{1,2,a)} Winnie Wong-Ng ² Vladimir Oleshko ² Gery R. Stafford ² James A. Kaduk ^{3,4} Andreza Eufrazio,⁵ Ian L. Pegg,^{1,5} and Bipradas Dutta¹

¹Physics Department, The Catholic University of America, Washington, DC 20064, USA

²Materials Measurement Laboratory, National Institute of Standards and Technology, Gaithersburg, MD 20899, USA

³Department of Physics, North Central College, Naperville, IL 60540, USA

⁴Department of Chemistry and Biochemistry, Illinois Institute of Technology, Chicago, IL 60616, USA

⁵Vitreous State Laboratory, The Catholic University of America, Washington, DC 20064, USA

(Received 8 December 2023; accepted 7 May 2024)

Crystal structures, microtopography, morphologies, elemental compositions, and ionic conductivity have been investigated for $\text{Li}_{5-x}\text{La}_3(\text{Nb,Ta})\text{O}_{12-y}$ using X-ray diffraction (XRD), field-emission analytical scanning and transmission electron microscopies (S/TEM), and electrochemical impedance spectroscopy. Using Rietveld refinements with powder XRD patterns, we determined that the number of Li atoms in the formula is less than 5 and that $\text{Li}_{5-x}\text{La}_3(\text{NbTa})\text{O}_{12-y}$ crystallizes in the cubic garnet structure with a space group *Ia-3d*. Sintering at varying temperatures (750–1000 °C) for 5 h in an ambient atmosphere produced distinct outcomes. Rietveld refinements disclosed that the sample sintered at 1000 °C ($\text{Li}_{3.43(2)}\text{La}_3\text{Nb}_{1.07(2)}\text{Ta}_{0.93(2)}\text{O}_{12-y}$, $a = 12.8361(7)$ Å, $V = 2114.96(3)$ Å³) exhibited the highest ionic conductivity, while the 850 °C sample had the lowest conductivity, characterized by lower Li concentration and impurity phases ($\text{Li}(\text{Nb,Ta})_3\text{O}_{88}$, Li_2CO_3). Analyses, including XRD and electron microscopy, confirmed the 1000 °C sample as a relatively phase pure with enhanced Li content (Li/La = 1.2), larger grains (15 µm), and uniform crystallinity. The 1000 °C sample introduced additional partially filled Li3 (96h) sites, promoting Li migration, and enhancing ionic conductivity. The resulting XRD pattern at 1000 °C has been submitted to the Powder Diffraction File as a reference.

© The Author(s), 2024. Published by Cambridge University Press on behalf of International Centre for Diffraction Data. This is an Open Access article, distributed under the terms of the Creative Commons Attribution licence (<http://creativecommons.org/licenses/by/4.0/>), which permits unrestricted re-use, distribution and reproduction, provided the original article is properly cited. [doi:10.1017/S0885715624000290]

Key words: $\text{Li}_{5-x}\text{La}_3(\text{NbTa})\text{O}_{12-y}$, solid electrolyte, X-ray diffraction patterns, STEM, EELS, ionic conductivity

I. INTRODUCTION

Rechargeable lithium-ion batteries (LIBs) offer high energy density and a long lifetime, and hence, they are considered the preferred electric energy and power sources for electric and hybrid vehicles, smartphones, computers, laptops, circuit cards, and other portable devices as well as for large stationary energy grid storage systems (Ramzy and Thangadurai, 2010; Mizuno et al., 2013; Kotobuki and Koishi, 2014). In the past, the deployment of electric cars and wireless communications, which dated from the end of the 19th century, was slowed mainly on account of the paucity of good batteries with suitable electrode materials and electrolytes and the associated difficulties in mastering the interfaces between them. So, in 1899, at an international car competition in Paris, the only petrol-driven car was disqualified for having impractically high consumption. The proportion of electric

cars produced in the U.S. between 1900 and 1920, however, fell from 60 to 4% of the total as they were replaced with affordable gasoline-powered cars such as the mass-produced Ford Model T (Mauger et al., 2019). Nowadays, high energy densities (over 400 Wh kg⁻¹) are required for emerging applications in electrical transportation, such as electric vehicles with large driving ranges of 500 km or more, long-endurance unmanned aerial systems, and space exploration. These requirements continue to push batteries to the performance limit, and at the same time, require them to remain safe, environmentally friendly, and reliable through hundreds or thousands of rapid charge–discharge cycles. Liquid and polymer electrolytes, which are currently used in LIBs, lack thermal stability and are also highly flammable, posing serious safety concerns (Goodenough and Park, 2013; Dhivya and Murugan, 2014). With all the problems of liquid electrolytes faced by the contemporary battery industry, there is a strong desire to develop all-solid-state Li-ion batteries (ASSLIBs) with inorganic solid-state electrolytes. A variety of highly conductive solid-state ionic electrolytes in crystalline, as well as

^{a)} Author to whom correspondence should be addressed. Electronic mail: kafle@cua.edu



noncrystalline forms, have been studied. Examples of such electrolytes include NASICON (Na Super Ionic Conductor), and various solids in different crystalline forms such as garnets, perovskites sulfides, and argyrodites (Bachman et al., 2016). Extensive research has been carried out in garnet type ceramics with a variety of crystal structures that can be considered potential superionic solid-state electrolytes for ASSLIBs. Moreover, they provide chemical and thermal stability against the lithium metal anode with a wide electrochemical stability window of 0–9 V (Zheng et al., 2018), which is another important criterion desired for the development of the next-generation high-energy-density ASSLIBs.

The general chemical formula of an ideal garnet is $A_3B_2(XO_4)_3$ where $A = \text{Ca, Mg, Y, La, or rare-earth metals}$; $B = \text{Al, Fe, Ga, Ge, Mn, Ni, or V}$; and $X = \text{Si, Ge, and Al}$. In the $A_3B_2(XO_4)_3$ structure (cubic $Ia-3d$ (Thangadurai et al., 2014)), A , B , and X are eight (antiprismatic, $24c$), six (octahedral $48g$), and four (tetrahedral $24d$) oxygen-coordinated cation sites, respectively. O'Callaghan et al. (2006) synthesized the compounds $\text{Ln}_3\text{Te}_2(\text{LiO}_4)_3$, $\text{Li}_3\text{Ln}_3\text{Te}_2\text{O}_{12}$, ($\text{Ln} = \text{Y, Pr, Nd, Sm-Lu}$) to investigate the structure and ionic-transport properties. It was demonstrated that these compounds adopt the garnet structure with lattice parameters in the range 12.1597(14) Å ($\text{Li}_3\text{Lu}_3\text{Te}_2\text{O}_{12}$) to 12.6159(7) Å ($\text{Li}_3\text{Pr}_3\text{Te}_2\text{O}_{12}$), where Li ions appear only in the tetrahedral ($24d$) sites in the space group $Ia-3d$. The conventional garnets $\text{Li}_3\text{Gd}_3\text{Te}_2\text{O}_{12}$, $\text{Li}_3\text{Tb}_3\text{Te}_2\text{O}_{12}$, $\text{Li}_3\text{Er}_3\text{Te}_2\text{O}_{12}$, and $\text{Li}_3\text{Lu}_3\text{Te}_2\text{O}_{12}$ have demonstrated considerably lower conductivity values, approximately $4.4 \times 10^{-6} \text{ S cm}^{-1}$ at a temperature of 285 °C, and their activation energies range from 0.77(4) to 1.21(3) eV (Cussen et al., 2011). Thangadurai et al. (2003) were the first to report the garnet compounds, $\text{Li}_5\text{La}_3\text{M}_2\text{O}_{12}$ ($M = \text{Nb, Ta}$). Both the niobium and tantalum members have bulk ionic conductivities around $10^{-6} \text{ S cm}^{-1}$ at 25 °C with the activation energies for ionic conduction (<300 °C) 0.43 and 0.56 eV for $\text{Li}_5\text{La}_3\text{Nb}_2\text{O}_{12}$ and $\text{Li}_5\text{La}_3\text{Ta}_2\text{O}_{12}$, respectively. In fact, in some Li-stuffed garnets, the excess Li atoms fill octahedral sites in the garnet structure, increasing Li-ion conduction, suggesting that Li in the tetrahedral sites might be less mobile than those in the octahedral sites (Cussen, 2006). The crystal structure of the compound with the general formula $\text{Li}_5\text{La}_3\text{M}_2\text{O}_{12}$ ($M = \text{Nb, Ta}$) is recognized as the garnet-like structure ($a = 12.889(3)$ Å for $M = \text{Nb}$ and 12.823(2) Å for $M = \text{Ta}$) with the space group $Ia-3d$ (Thangadurai et al., 2003). The infinite chains of $(\text{La}_3\text{M}_2\text{O}_{12})_n$ – are arranged in four different directions. The chains share lanthanum and lithium atoms to have a strong connection among themselves (Hyooma and Hayashi, 1988). Furthermore, $\text{Li}_5\text{La}_3\text{Ta}_2\text{O}_{12}$ appears to have more chemical and thermal stability, particularly in contact with molten metallic lithium, than $\text{Li}_5\text{La}_3\text{Nb}_2\text{O}_{12}$ (Thangadurai et al., 2004). To date, many efforts have been undertaken to optimize Li-ion conductivity with a variety of substitutions in the Ta/Nb sites (Narayanan et al., 2012; Baral et al., 2014; Nemori et al., 2014).

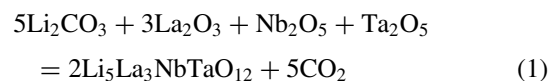
The first goal of our work was to study the influence of the sintering temperature on the structure and ionic conductivity of the garnet-type compound $\text{Li}_{5-x}\text{La}_3(\text{NbTa})\text{O}_{12-y}$ as prospective electrolyte for ASSLIBs. The sintering temperatures of our compounds ranged from 750 to 1000 °C (discussed below). Crystal structures and grain morphologies of these samples were determined using the X-ray Rietveld refinement and analytical scanning and transmission electron microscopy

(S/TEM) methods. Their ionic conductivity values were measured using electrochemical impedance spectroscopy. Furthermore, to our knowledge, only limited reports in the literature have discussed the Li site content (Paoella et al., 2020). Most reports only assume their materials contain 5 Li atoms per formula unit. In general, refining Li positions and occupancies in the presence of higher Z elements such as La, Nb, and Ta is expected to be difficult with XRD patterns. Neutron diffraction which probes the positions of atomic nuclei directly can provide more accurate information about locations within the crystal structure. In our case, we are interested in Li content so we attempted to obtain the Li content and locations using the Rietveld refinement technique and compare the Li/La atomic ratio values with data obtained by spatially resolved electron energy-loss spectroscopy (STEM-EELS). Furthermore, since X-ray diffraction (XRD) is a nondestructive technique for phase identification, XRD patterns are especially important for phase characterization. Therefore, the second goal of this investigation was to determine the experimental powder reference pattern for $\text{Li}_5\text{La}_3\text{NbTaO}_{12}$ sintered at 1000 °C, which has the optimum ionic conductivity among the series, and to make it widely available through submission to the Powder Diffraction File (PDF) (Gates-Rector and Blanton, 2019).

II. EXPERIMENTAL

A. Materials synthesis

A master batch of the garnet compound based on the nominal composition, $\text{Li}_5\text{La}_3\text{NbTaO}_{12}$, was first prepared by the conventional solid-state reaction method.



The precursor chemicals Li_2CO_3 (5% excess, Alfa Assar, 99.9% purity), (The purpose of identifying the equipment, software, or chemicals in this article is to specify the experimental procedure. Such identification does not imply recommendation or endorsement by the National Institute of Standards and Technology) La_2O_3 (Alfa Assar, purity: 99.8%, preheated at 750 °C for 15 h), Nb_2O_5 (Sigma-Aldrich, purity: 99.9%), and Ta_2O_5 (Sigma-Aldrich, purity: 99.9%) were weighed according to the required stoichiometry ratio. The chemicals were mixed thoroughly and set for wet ball milling with isopropanol in an alumina jar and alumina balls, size 8 mm with 1:8 mass ratio, precursors mixture to balls, for 12 h at a frequency of 45 Hz using Planetary Ball Milling Machine (PQN04) (The purpose of identifying the equipment, software, or chemicals in this article is to specify the experimental procedure. Such identification does not imply recommendation or endorsement by the National Institute of Standards and Technology). The powder, collected after drying at 60 °C for 24 h, was pressed into pellets with dry pressing under the load of 3 tons for 2 min. The pellet on an alumina plate was placed into the electric furnace at 750 °C for 5 h in an ambient atmosphere. After heating, the pellet was crushed into powder, and the previous procedures from ball milling to heat treatment were repeated. The powder obtained after the second heating was used as a master batch to further prepare various pellets of 10 mm diameter and

sintered at different temperatures: 750, 800, 850, 900, 950, and 1000 °C for 5 h each in air. The sintered pellets were then used for further characterization and impedance measurements. For labeling convenience, in the following discussion, the samples with final sintering temperatures at 750, 800, 850, 900, 950, and 1000 °C are referred to as L750, L800, L850, L900, L950, and L1000, respectively.

B. X-ray diffraction

For powder XRD and S/TEM analyses, the pellets described above were crushed to produce a powder. Preliminary phase characterizations were performed using a computer-controlled Rigaku SmartLab-SE Θ – Θ X-ray diffractometer at 10 to 60° 2θ , 1° per min, with Cu $K\alpha$ radiation (wavelength of 1.5406 Å). The powder XRD patterns for Rietveld refinement studies were measured on a PANalytical Empyrean Debye-Scherrer diffractometer equipped with an incident-beam focusing mirror and an X'Celerator detector. The patterns (1° to 100° 2θ , 0.0083557° per step, 4 s per step, 1/4° divergence slit, 0.02 radian Soller slits) were measured using Mo $K\alpha$ radiation with the wavelength 0.7107 Å. The powder specimen was contained within a 0.3 mm diameter glass capillary tube.

The Rietveld refinement technique (Rietveld, 1969), along with the software suite GSAS-II (Toby and Von Dreele, 2013), was used to refine the structure of the four $\text{Li}_{5-x}\text{La}_3(\text{Nb,Ta})\text{O}_{12-y}$ samples (L750, L850, L950, and L1000). As discussed below, two compositions of the series, namely, L750 and L1000, have been studied in more detail. The reference powder XRD patterns were also obtained for these two samples using a Rietveld pattern decomposition technique. The reported peak intensities were derived from the extracted integrated intensities, and positions were calculated from the lattice parameters. For peaks that cannot be resolved, the intensities are summed, and an intensity-weighted d -spacing is reported. From the full width at half maximum (FWHM) of the diffraction peaks and the profile parameters, we also modeled the broadening with micro strain (assuming the sizes were 1 μm (effectively infinite).

C. Scanning and transmission electron microscopy (SEM/TEM)

For SEM measurements, a piece of a sintered pellet was cut and mounted on an aluminum alloy sample stub holder and coated with carbon. SEM of the carbon-coated samples was carried out with a JEOL JSM 6300 scanning electron microscope using 10 kV accelerating voltage. Uncoated ceramic powders were characterized using a Helios NanoLab 660 dual-beam focused ion beam/scanning electron microscope (FIB/FESEM, ThermoFisher Scientific) equipped with a Schottky thermal field emission gun and a high-speed silicon-drifted (SDD) energy-dispersive X-ray (EDX) Oxford Instruments X-Max 80 mm² detector. For FESEM and EDX analyses, the specimens were mounted on standard aluminum alloy stubs covered with conductive carbon adhesive tape. FESEM imaging was conducted at accelerating voltages of 1, 5, and 10 kV, beam currents of 50–100 pA, and a working distance of 2–7 mm with high-performance Everhart–Thornley (ETD) and in-length (TLD) secondary electron (SE) or backscattered electron (BSE) detectors.

Since the samples were insulated and analyzed without any conductive coating, a stage bias of 50 V was applied to mitigate severe charging effects. FESEM imaging was carried out at several magnifications ranging from wide-field views at $\times 100$ to $\times 2000$ to ensure the measurements were reproducible and statistically representative. Utilizing a high-speed large-area SDD EDX detector and an Aztec microanalysis system (Oxford Instruments NanoAnalysis) under a computerized control of imaging parameters, pixel-by-pixel spectral acquisition, and live time data processing, true real-time X-ray spectroscopic imaging (SI) of the samples was conducted at 5 and 10 kV accelerating voltage to characterize elemental distributions of ceramic powders. Low-dose transmission electron microscopy (TEM) in bright-field (BF) mode, selected-area electron diffraction (SAED), and phase-contrast high-resolution TEM (HRTEM) imaging were performed using a Schottky field-emission Titan 80-300 TEM (Thermo Fischer Scientific) with a point-to-point resolution of 0.19 nm at 300 kV accelerating voltage equipped with a Super-TWIN objective lens, and a OneView IS 4 k \times 4 k high-speed CMOS camera (AMETEK (Gatan)). The instrument was operated at minimal beam illumination levels with doses down to 100 e/nm² to reduce radiation damage to the samples. Scanning TEM (STEM) using BF and high-angle annular dark-field (HAADF) modes, electron energy-loss spectroscopy (EELS), and EDX spectroscopic imaging of the powder samples was carried out with a probe-corrected Titan 80-300 (ThermoFisher Scientific) scanning transmission electron microscope at 300 kV accelerating voltage. For S/TEM measurements, ceramic powders were deposited onto lacey carbon 200 Cu mesh grids. No staining agents were used to enhance the contrast of the TEM images.

D. Electrochemical impedance spectroscopy

For electrochemical impedance spectroscopy (EIS) studies, sintered pellets were prepared for L750, L800, L850, L900, L950, and L1000. Silver electrical contacts were applied to both sides of the sintered pellets by thermal evaporation of silver metal. The silver-deposited pellet was secured between two copper plates, and the assembly was inserted into a custom-built sample holder. Impedance measurements were made on the silver-deposited pellets using a two-probe technique, an Autolab PGSTAT302 potentiostat (Metrohm), and NOVA 1.9 software. The impedance measurements were carried out in the 100 kHz to 0.1 Hz frequency range at a 100 mV RMS AC signal. The impedance was measured under vacuum at 25, 45, 65, and 85 °C. The total ionic conductivity of each pellet was calculated from the resistance values obtained by fitting the impedance data (Lazanas and Prodromidis, 2022) to an appropriate equivalent circuit, and normalized to the sample geometry.

III. RESULTS AND DISCUSSION

A. X-ray powder diffraction analysis

The results of XRD structural analyses of the four samples agree with the structure of the two end-members with compositions $\text{Li}_5\text{La}_3\text{M}_2\text{O}_{12}$ (Thangadurai et al., 2004; Murugan et al., 2006; Geiger et al., 2011), namely, cubic with the space group $1a\text{-}3d$ $\text{Li}_5\text{La}_3\text{Ta}_2\text{O}_{12}$ (PDF4: 01-086-5324).

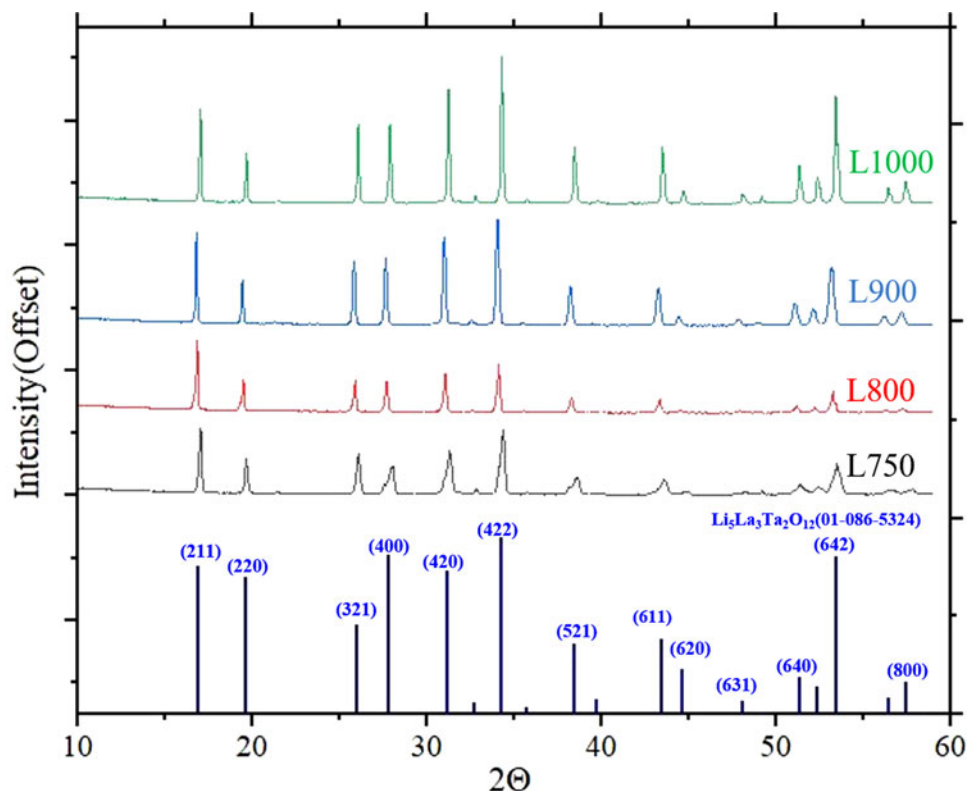


Figure 1. Powder XRD patterns of $\text{Li}_{5-x}\text{La}_3\text{NbTaO}_{12-y}$ heat-treated at 750, 800, 900, and 1000 °C, measured using $\text{Cu } K\alpha$ radiation at room temperature. The bottom XRD stick patterns referring respective $[hkl]$ values correspond to the PDF pattern (01-086-5324) for $\text{Li}_3\text{La}_3\text{NbTaO}_{12}$ (Gates-Rector and Blanton, 2019).

Considering the fact that the peak intensities are dependent on Z^2 so the refinement of Li ($Z=3$) site occupancy is challenging in the presence of La ($Z=57$), and Ta ($Z=73$), we have tried different starting models. Finally, we have successfully refined the Li occupancy using the Rietveld method with “stable” results (convergent least-squares refinements). As discussed below, the resulting samples sintered at 750, 850, 950, and 1000 °C were all Li-deficient.

Selected X-ray patterns of the powder specimen of $\text{Li}_{5-x}\text{La}_3(\text{Nb,Ta})\text{O}_{12-y}$ series heat-treated from 750 to 1000 °C are shown in Figure 1. All these patterns match well with that of the cubic $\text{Li}_3\text{La}_3\text{Ta}_2\text{O}_{12}$ type; barring the presence of some minor impurity phases. The results of Rietveld refinements for the $\text{Li}_{5-x}\text{La}_3(\text{Nb,Ta})\text{O}_{12-y}$ series are shown in Table I and Figure 2. Table I gives the statistical agreement factors or residual values, R and wR , whereas, in Figure 2, the observed (crosses), calculated (solid line), and difference XRD patterns (bottom) for L1000 are illustrated. The normalized difference pattern is provided. Above $45^\circ 2\theta$, the vertical scale has been magnified by a factor of five. The row of tick marks indicates the calculated peak positions.

Table I also summarizes the nominal chemical formula and the lattice parameters based on XRD data obtained at 302(1) K. The following results are noted: (1) Li content is deficient in all samples, particularly for L850 ($\text{Li}_{1.7}\text{La}_3\text{Nb}_{1.07(2)}\text{Ta}_{0.93(2)}\text{O}_{12-y}$); (2) Impurity phases present in samples L750 ($\text{Li}(\text{Nb,Ta})_3\text{O}_8$ (0.59%) and Li_2CO_3 (4.2%)), L850 ($\text{Li}_8(\text{Nb,Ta})_2\text{O}_9$, 0.9% and Li_2CO_3 , 5.2%); and L950 ($\text{Li}_8(\text{Nb,Ta})_2\text{O}_9$, 3.7% and Li_2CO_3 , 3.3%); (3) L1000 ($\text{Li}_{3.43(2)}\text{La}_3\text{Nb}_{1.07(2)}\text{Ta}_{0.93(2)}\text{O}_{12-y}$) did not show visible impurity phases; (4) Samples annealed at $T > 800^\circ\text{C}$ appear to have slightly more Nb than Ta, probably due to the presence of impurity amorphous oxide phases containing slightly more Ta at higher temperature, i.e., $\text{Li}_8(\text{Nb,Ta})_2\text{O}_9$. Therefore, there appears to be a deficiency of Ta in $\text{Li}_{(5-x)}\text{La}_3(\text{Nb,Ta})\text{O}_{12-y}$; (5) The presence of the impurity phases gave rise to the somewhat high values of R and wR values in Table I; (6) There does not seem to be a well-defined trend about the lattice parameters, temperature at which the samples were heat-treated and the Li content. For Rietveld refinements, we fixed both the La and O contents (need to fix at least one variable during the refinement process). In reality, there may be a small variation

TABLE I. Rietveld refinement results (R and wR values) and lattice parameter for $\text{Li}_{5-x}\text{La}_3(\text{Nb,Ta})\text{O}_{12-y}$ sintered at different temperatures.

| Sintering temp (°C) | Chemical formula | a (Å) | V (Å ³) | R (%) | wR (%) |
|---------------------|---|-------------|-----------------------|---------|----------|
| 750 | $\text{Li}_{2.77(2)}\text{La}_3\text{Nb}_{1.03(2)}\text{Ta}_{0.97(2)}\text{O}_{12-y}$ | 12.82719(6) | 2110.54(3) | 5.98 | 7.66 |
| 850 | $\text{Li}_{1.7}\text{La}_3\text{Nb}_{1.07(2)}\text{Ta}_{0.93(2)}\text{O}_{12-y}$ | 12.8448(2) | 2119.26(10) | 7.8 | 12.3 |
| 950 | $\text{Li}_{2.62}\text{La}_3\text{Nb}_{1.11(2)}\text{Ta}_{0.89(2)}\text{O}_{12-y}$ | 12.8668(15) | 2130.16(9) | 5.81 | 7.98 |
| 1000 | $\text{Li}_{3.43(2)}\text{La}_3\text{Nb}_{1.07(2)}\text{Ta}_{0.93(2)}\text{O}_{12-y}$ | 12.8361(7) | 2114.96(3) | 5.44 | 7.12 |

Values inside brackets are one standard deviation.

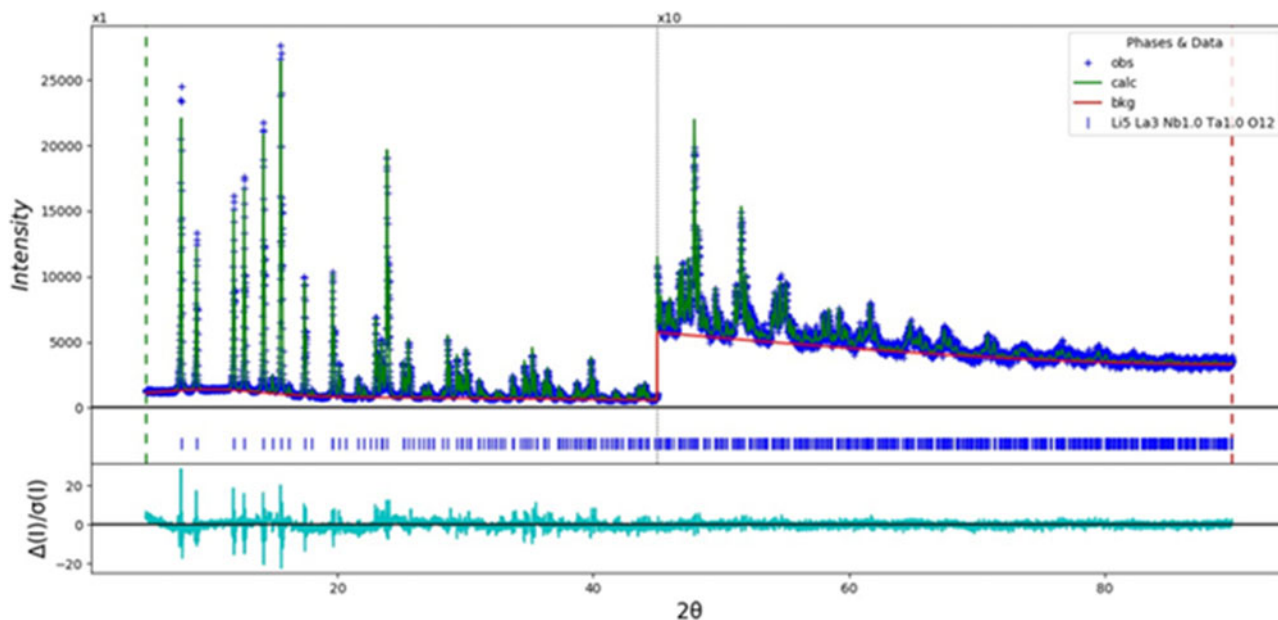


Figure 2. Observed (crosses, blue color), calculated (solid line, green color), and difference XRD patterns (bottom, bluish green color) for L1000 ($\text{Li}_{3.43(2)}\text{La}_3\text{Nb}_{1.07(2)}\text{Ta}_{0.93(2)}\text{O}_{12-y}$); the difference pattern is plotted using the same vertical scale across the entire 2θ range. Above $45^\circ 2\theta$, the vertical scale has been magnified by a factor of five. The row of tick marks indicates the calculated peak positions.

TABLE II. Full width at half maximum (FWHM) of the first peak of the powder pattern of $\text{Li}_{5-x}\text{La}_3(\text{NbTa})_2\text{O}_{12}$ with average strain, ppm at different temperatures.

| T ($^\circ\text{K}$) | 750 | 800 | 850 | 900 | 950 | 1000 |
|--------------------------|-------|-------|-------|-------|-------|-------|
| FWHM ($^\circ$) | 0.068 | 0.087 | 0.098 | 0.081 | 0.090 | 0.065 |
| Average strain (ppm) | 1936 | 6384 | 7084 | 4868 | 9454 | 4018 |

of the La and O content which may affect the lattice parameters. Moreover, if there are small oxygen content change and coordination number change around Nb^{5+} and Ta^{5+} , this would only be local effect, affecting the local structure. XRD captures the average structure and will not be able to provide information about the local structure. Detailed investigation about the local structure including the change in the coordination number of Nb^{5+} and Ta^{5+} and oxygen vacancy is beyond the scope of this study.

The FWHM values of the first peak in all samples are given in Table II. These results indicated that the FWHM values are the smallest for L750 and L1000 whereas the strain values have the same trend. All these values correlate well with the grain size, namely, the smaller the FWHM, the smaller the strain value and the larger the grain, as demonstrated by the SEM photographs.

Tables III and IV provide the atomic coordinates for samples L750 and L1000. Relevant bond distances of L750 and L1000 are presented in Table V. Figure 3 depicts the general structure of $\text{Li}_{5-x}\text{La}_3(\text{NbTa})\text{O}_{12-y}$ featuring the LiO_4 , LiO_6 , and $(\text{Nb/Ta})\text{O}_6$ polyhedrons, except for Li3 for L1000. Figure 4 illustrates the LaO_8 antiprisms. The Li sites in some of these polyhedrons are deficient due to Li evaporation. It is noted that the Li atoms in the structures of L750 and L1000 occupy the same two main sites with similar occupancy, namely, the Li1 tetrahedral site (24d) and the Li8 octahedral site (16b). It seems that Li sites could move around as a function of temperature. Although we located a possible Li2 site (48g) with coordinates (0.125, 0.687(2), 0.563), its occupancy factor is very small (0.03(2)), which is practically zero taking into consideration of the standard deviation. On the other hand, the additional Li3 in L1000 occupies a 96h position (in this case a disordered site for Li) enabling a greater number of sites for Li migration, as compared to the samples heat-treated at lower temperatures, possibly leading to increased conductivity. Figures 5 and 6 illustrate the distribution of Li sites, Li1 and Li8 in L750 and Li1, Li3, and Li8 in L1000, respectively. The Li3–O7 distances were found to be 2.42(2) Å, 1.98(2) Å, and 1.99(2) Å.

The powder XRD pattern for $\text{Li}_{3.43(2)}\text{La}_3\text{Nb}_{1.07(2)}\text{Ta}_{0.93(2)}\text{O}_{12-y}$ has been submitted for inclusion in the PDF.

TABLE III. Atomic coordinates of L750 ($\text{Li}_{2.77(2)}\text{La}_3\text{Nb}_{1.03(2)}\text{Ta}_{0.97(2)}\text{O}_{12-y}$, sintered at 750 $^\circ\text{C}$).

| Atom | x | y | z | Occ | U_{iso} | Wyck _{off} |
|------|-----------|-----------|-----------|----------|---------------------|---------------------|
| Li1 | 0.250 | 0.875 | 0.000 | 0.78(3) | 0.0200 | 24d |
| La4 | 0.125 | 0.000 | 0.250 | 1.000 | 0.0169 ^a | 24c |
| Nb5 | 0.000 | 0.000 | 0.000 | 0.514(3) | 0.0189(2) | 16a |
| Ta6 | 0.000 | 0.000 | 0.000 | 0.486(3) | 0.0189(2) | 16a |
| O7 | 0.2842(2) | 0.1068(2) | 0.2011(2) | 1.00 | 0.0186(11) | 96h |
| Li8 | 0.125 | 0.125 | 0.125 | 0.14(3) | 0.0200 | 16b |

Values inside brackets are one standard deviation.

^aU11, U22, U33, U12, U13, and U23 components are 0.0161(6), 0.0172(3), 0.0172(3), 0.0, 0.0, and 0.0034(9).

TABLE IV. Atomic coordinates of L1000 ($\text{Li}_{3.43(2)}\text{La}_3\text{Nb}_{1.07(2)}\text{Ta}_{0.93(2)}\text{O}_{12-y}$, sintered at 1000 °C).

| Atom | x | y | z | Occ | U_{iso} | Wyck _{off} |
|------|----------|----------|----------|-----------|---------------------|---------------------|
| Li1 | 0.250 | 0.875 | 0.000 | 0.78(3) | 0.0200 | 24d |
| Li3 | 0.095(2) | 0.678(2) | 0.566(2) | 0.069(15) | 0.0200 | 96h |
| La4 | 0.125 | 0.000 | 0.250 | 1.00 | 0.0190 ^a | 24c |
| Nb5 | 0.000 | 0.000 | 0.000 | 0.536(3) | 0.0218(2) | 16a |
| Ta6 | 0.000 | 0.000 | 0.000 | 0.464(3) | 0.0218(2) | 16a |
| O7 | 0.281(2) | 0.107(2) | 0.199(2) | 1.000 | 0.0160(1) | 96h |
| Li8 | 0.125 | 0.125 | 0.125 | 0.13(3) | 0.0200 | 16b |

Values inside brackets are one standard deviation.

^aU11, U22, U33, U12, U13, and U23 components are 0.0175(6), 0.0197(4), 0.0197(4), 0.0, 0.0, and 0.0026(10).

TABLE V. Relevant bond distances (Å) in $\text{Li}_{5-x}\text{La}_3(\text{NbTa})\text{O}_{12-y}$.

| | L750 | L1000 |
|------------|--------------|--------------|
| La4–O7 | 2.538(3) × 4 | 2.520(3) × 4 |
| | 2.628(3) × 4 | 2.601(3) × 4 |
| Li1–O7 | 1.904(2) × 4 | 1.939(3) × 4 |
| Li3–O7 | | 2.42(2) |
| | | 1.98(2) |
| | | 1.99(2) |
| | | 1.98(2) |
| Li8–O7 | 2.276(2) × 6 | 2.235(3) × 6 |
| Nb5/Ta6–O7 | 1.990(2) × 6 | 1.986(2) × 6 |

Values inside brackets are one standard deviation.

B. Analytical FESEM and S/TEM

SEM images of powder pellets L750 and L1000 in Figures 7(a) and 7(b), respectively, demonstrated tightly packed agglomerated grains with significantly varying morphologies produced during densification of the pellets under 3 tons of load. Because of the dense packing and morphological complexity, it was, however, sometimes difficult to distinguish individual particles and grain facets. On the other hand, a series of FESEM and STEM images of the powders in Figures 7(c)–7(h) and Figures 7(i)–7(j), respectively, evidently display larger individual grains with faceting in the

sample L1000 as compared to L750. Furthermore, to characterize the chemical compositions of the garnets, analytical FESEM was performed at accelerating voltages of 1, 5, and 10 kV on as-received uncoated powders in field-free and immersion modes applying a 50 V deceleration bias to reduce severe beam-induced charging of the insulating samples. Figure 8 presents the results of FESEM observations of the L1000 garnet powder using SE₁, SE₂, and BSE (composition) signals combined with high-speed EDX SI. Monte Carlo simulations of the beam–garnet ceramic interactions (Drouin et al., 2007) (see Figure 8, right insets) indicate that for the chosen operating conditions, the interaction volume was increased by more than an order of magnitude with accelerating voltage from 20 nm × 20 nm at 1 kV to about 600 nm × 600 nm at 10 kV. So, an image in Figure 8(a) acquired at a low accelerating voltage of 1 kV illustrates the surface topography of the ceramic powder due to primarily SE₁ electrons generated within a 20 nm thick utmost subsurface layer. At 5 kV [Figure 8(b)], one notices an edge enhancement effect, as well as a contrast increase with accelerating voltage and probe current due to the increasing contributions from the SE₂s induced by BSEs, generated deeper in the sample [Figures 8(b) and 8(c)]. Compositional BSE imaging at 10 kV accelerating voltage using 50 and 200 pA probe current [Figures 8(d) and 8(e), respectively] allowed us to reveal grain facets, otherwise essentially masked by a lower atomic

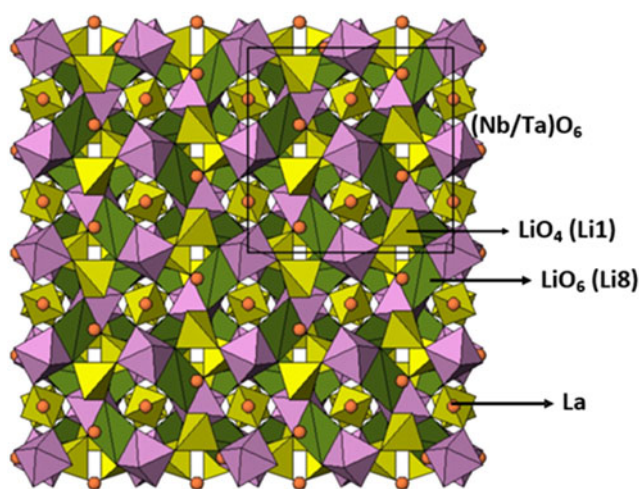


Figure 3. Structure of $\text{Li}_{5-x}\text{La}_3\text{NbTaO}_{12-y}$ (L1000 and L750), featuring the LiO_6 octahedrons, LiO_4 tetrahedrons, $(\text{Ta/Nb})\text{O}_6$ octahedrons, and La ions. A unit cell outline is provided in the upper right corner. Li3 in L1000 is not shown.

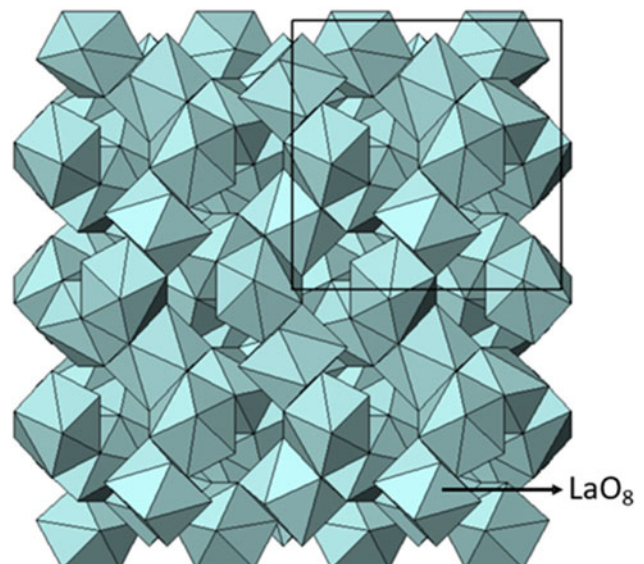


Figure 4. Structure of $\text{Li}_{5-x}\text{La}_3\text{NbTaO}_{12-y}$, featuring the LaO_8 antiprism. A unit cell outline is provided in the upper right corner.

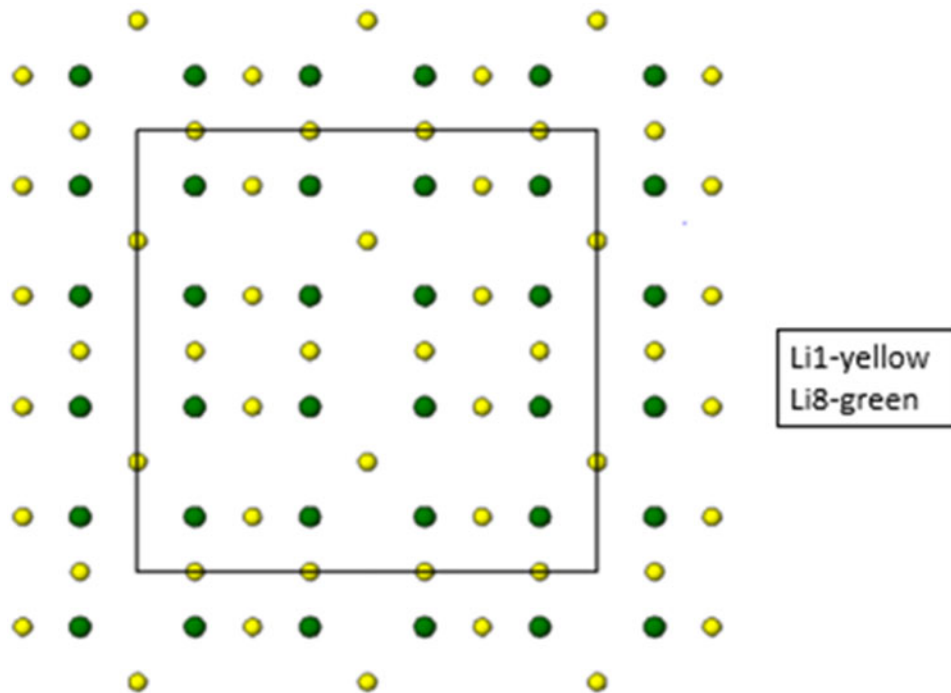


Figure 5. Locations of Li1 and Li8 in the unit cell of $\text{Li}_{5-x}\text{La}_3\text{NbTaO}_{12-y}$ heat-treated at 750 °C (Li1 – yellow and Li8 – green).

number phase, likely Li_2CO_3 , which often formed nonuniform shells around the grains. Corresponding X-ray elemental maps [Figures 8(f)–8(i)] acquired at 10 kV accelerating voltage and 200 pA probe current demonstrate oxygen (O–K), lanthanum (La–L), niobium (Nb–M), and tantalum (Ta–M) distributions. Finally, the results of chemical imaging are summarized in

Figures 8(j) and 8(k) which show a layered image composed of overlapped X-ray maps and SE signal and a map sum X-ray spectrum, respectively. In this way, multisignal FESEM combined with real-time chemical imaging enabled us to examine in detail rough surface microtopography, complex morphologies, and elemental distributions of the agglomerated garnet

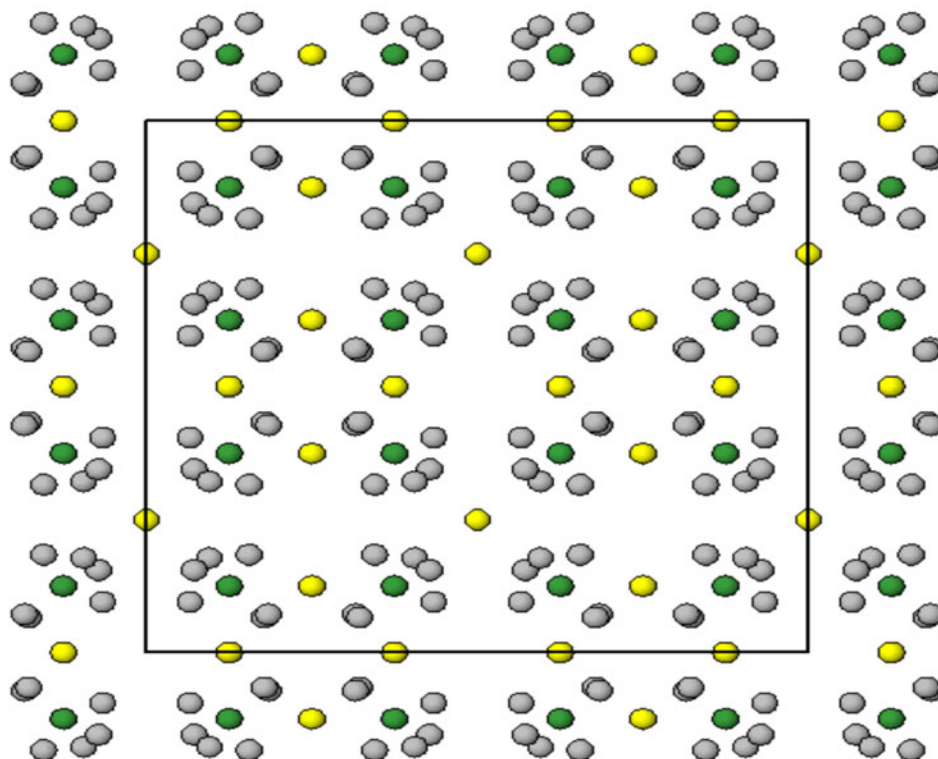


Figure 6. Locations of Li1, Li3, and Li8 in the unit cell of $\text{Li}_{5-x}\text{La}_3\text{NbTaO}_{12-y}$ heat-treated at 1000 °C (Li1 – yellow, Li3 – grey, and Li8 – green).

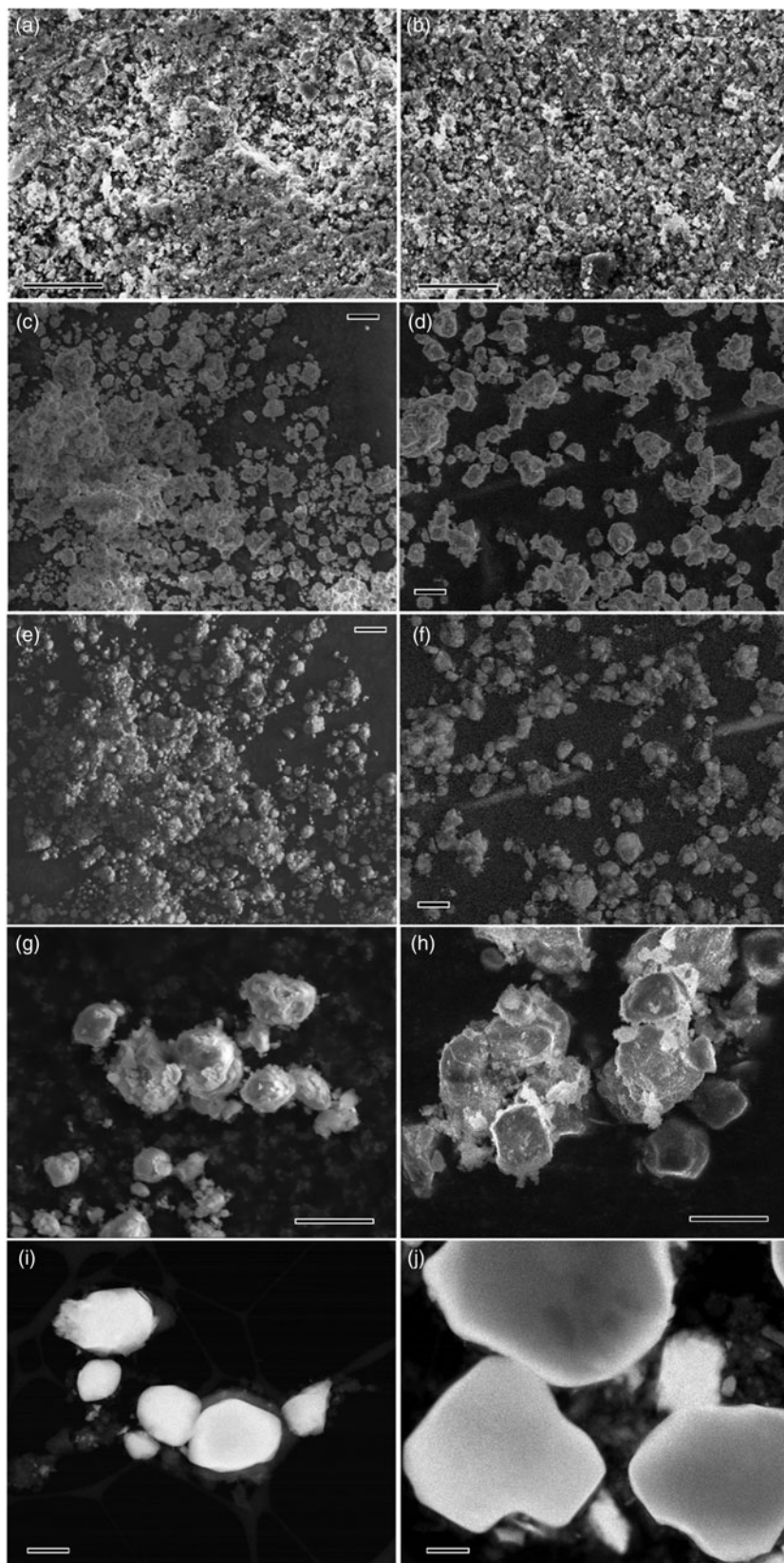


Figure 7. (FE)SEM and STEM comparison of the L750 garnet sample (left columns) and the L1000 garnet sample (right columns). (a and b) Secondary electron (SE₁ + SE₂) images of the pellets produced under pressure of 3 metric tons. Scale bars are 25 μm. (c and d) Large-area secondary electron (SE₁ + SE₂) images of the powders, (e and f) corresponding backscattered electron (BSE) composition images of the same areas. Scale bars are 10 μm. (g and h) Higher magnification secondary electron (SE₁ + SE₂) images of the powders. Scale bars are 5 μm. (i and j) HAADF STEM images of the powders. Scale bars are 1 μm.

powders with sizes ranging from 4 to 15 μm. The shapes of the grains gradually improved with sintering temperature from 750 to 1000 °C, displaying multiple facets and size growth.

The results of XRD phase analysis pointing to the high crystallinity of the garnet powders were directly corroborated at various structural levels using low-dose (down to 100 e/

nm²) TEM, SAED, and HRTEM. The BF-TEM image of the L1000 garnet sample in Figure 9(a) demonstrates heavily agglomerated powders with evidently faceted submicron-sized grains of various irregular shapes. The SAED pattern [top left inset, Figure 9(a)] shows point reflections corresponding to the cubic garnet phase near the [111] zone axis. The

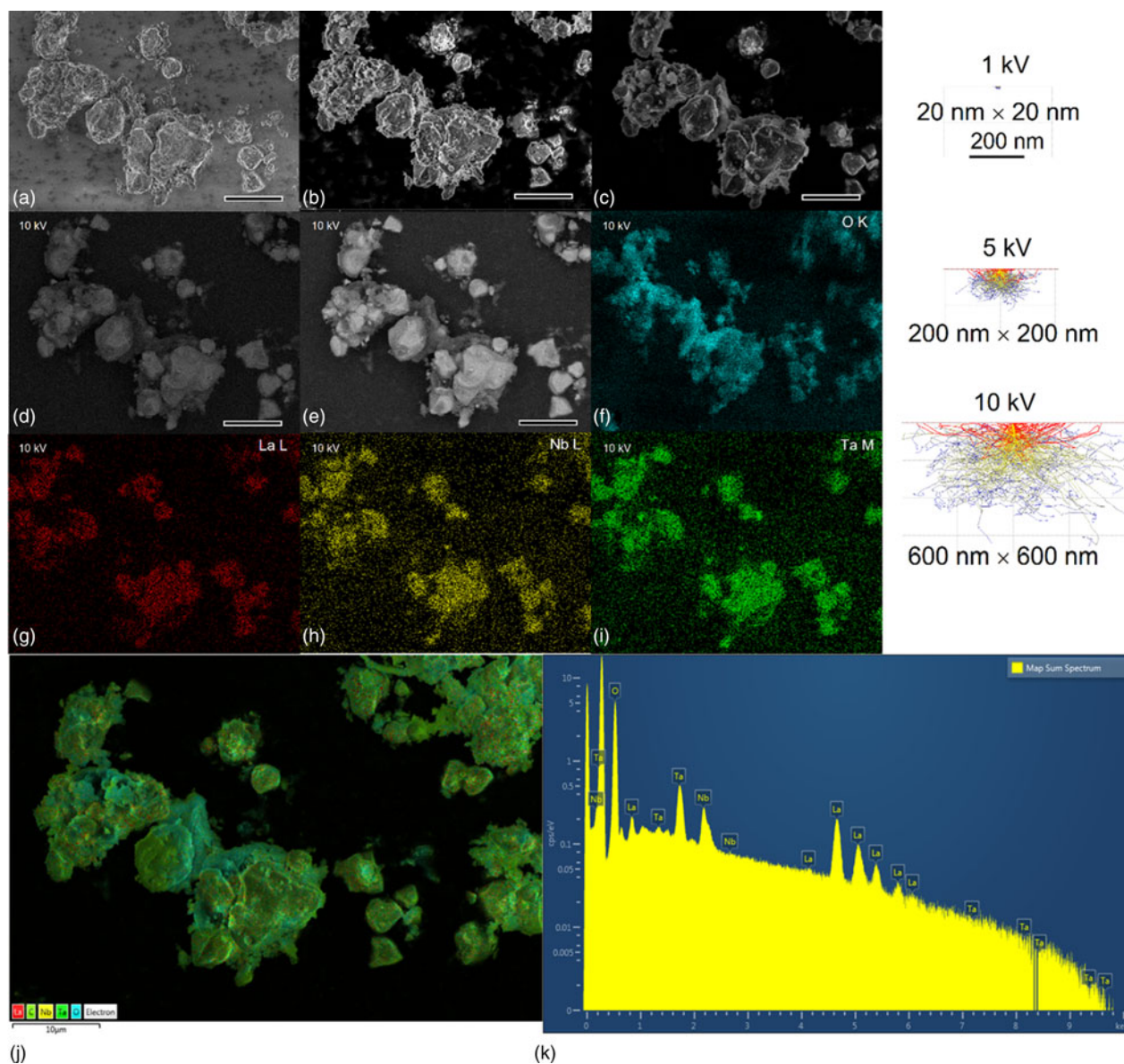


Figure 8. Multisignal analytical FESEM and EDX spectroscopic imaging (SI) of the L1000 powder, scale bars denote 10 μm . (a) Low-voltage secondary electron (SE_1) image, 1 kV accelerating voltage, 50 pA probe current. (b) Low-voltage SE_1 image, 5 kV accelerating voltage, 200 pA probe current. (c) Mixed signal immersion mode secondary electron ($\text{SE}_1 + \text{SE}_2$) image, 10 kV accelerating voltage, 50 pA probe current. (d) Immersion mode BSE composition image, 10 kV accelerating voltage, 50 pA probe current. (e) Immersion mode BSE composition image, 10 kV accelerating voltage, 200 pA probe current. (f) Oxygen O–K map, (g) lanthanum La–L map, (h) niobium Nb–L map, (i) tantalum Ta–M map, (j) a layered composite image showing the overlap of the LaL (red), NbL (yellow), TaM (green), and OK (cyan) X-ray maps and SE image, and (k) map sum X-ray spectrum shown in the log scale. The data were acquired at 10 kV accelerating voltage using a 200 pA probe current and 50 V bias. Left insets from top to bottom show Monte Carlo simulations of the beam–garnet ceramic interactions for the chosen operating conditions (1, 5, and 10 kV, 1 nm probe, 2000 trajectories, 0° tilt) performed with the Casino software package developed by Drouin et al. (2007). Scale bars are 200 nm. Trajectories of electrons that escaped the sample are shown in red.

HRTEM image in Figure 9(b) acquired at the edge of the garnet grain revealed 0.52 nm (211) and 0.34 nm (-321) lattice fringes, which, according to a Fast Fourier Transform (FFT) pattern [top inset, Figure 9(b)], were observed near the $[317]$ zone axis.

Lithium concentration is a critical parameter primarily responsible for stabilizing the cubic garnet phase and ionic conductivity of the electrolyte. Since EELS is well-suited to detect lithium due to the large ionization cross section of the Li K-edge at 55 eV energy loss (Egerton, 2011), STEM-EELS SI was employed to analyze lithium distributions in the garnet grains. Figures 10(a) and 10(b) present a HAADF STEM image of a grain fragment from the L1000

garnet sample and an EEL spectrum acquired over the area marked by the red box in Figure 10(a). The EEL spectrum with an assigned power-law background shows the Li K-edge at 55 eV and the delayed minor La $\text{N}_{4,5}$ -edge at about 115 eV energy loss. The La- $\text{N}_{4,5}$ edge is shifted by 10 eV to account for the delayed offset as expected for high-shell $4d^{5/2}$ and $4d^{3/2}$ electrons, e.g., see Paoletta et al. (2020). The Li K map and the La $\text{N}_{4,5}$ map acquired over the area are shown in Figures 10(c) and 10(d), respectively. The lithium-to-lanthanum atomic ratio was estimated by limiting measurements to thin crystallite areas with a thickness $t/\lambda < 0.5$ (here λ is the mean free electron path) to minimize plural scattering effects using the standard ratio quantification

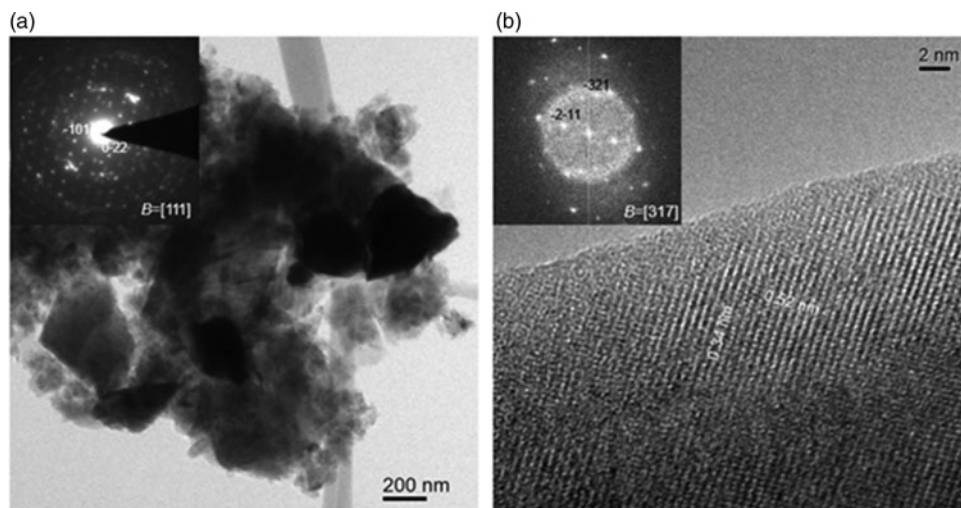


Figure 9. TEM images of L1000 garnet powder. (a) Bright-field (BF)-TEM micrograph of agglomerated garnet grains and selected-area diffraction (SAED) pattern (inset) acquired near the [111] zone axis. (b) High-resolution TEM (HRTEM) image demonstrating high crystallinity and (211) and (−321) lattice fringes at the edge of the grain and corresponding fast Fourier transform (FFT) pattern (inset) oriented near the [317] zone axis.

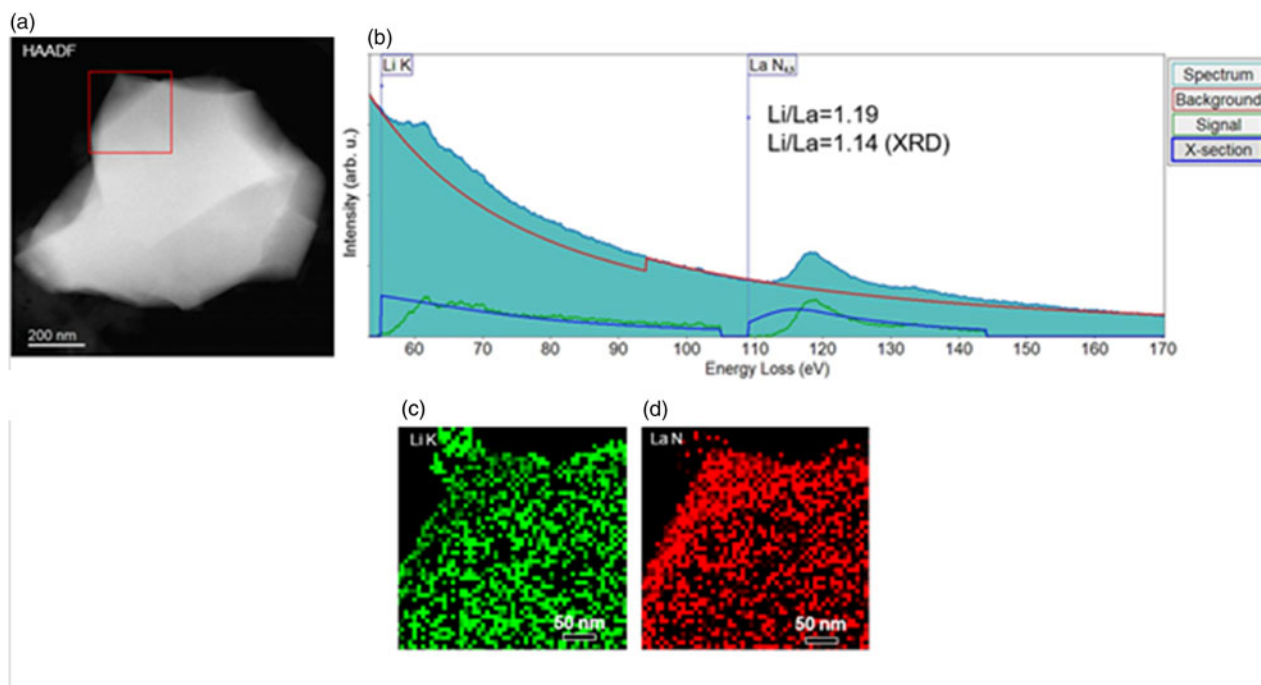


Figure 10. STEM-EEL SI of a grain fragment of the L1000 garnet powder. (a) HAADF STEM image of faceted powder grain. (b) EEL spectrum acquired over the area marked by the red box in (a) showing an assigned power-law background (red curve) and the Li K-edge at 55 eV and the delayed La $N_{4,5}$ -edge at about 115 eV. The net Li K edge and the net La $N_{4,5}$ edge are shown in green and the calculated Hartree-Slater ionization cross sections for the edges are shown in blue, respectively. (c and d) The Li K map (green) and the La $N_{4,5}$ map (red) acquired over the marked area.

method via Eq. (2) as described in Egerton (2011):

$$\begin{aligned} N_{\text{Li}}/N_{\text{La}} &= I_{\text{Li}}(a, \beta, \Delta E)/I_{\text{La}}(a, \beta, \Delta E) \\ &\times \sigma_{\text{La}}(a, \beta, \Delta E)/\sigma_{\text{Li}}(a, \beta, \Delta E), \end{aligned} \quad (2)$$

where N_{Li} and N_{La} are the numbers of Li and La atoms per unit area, I_{Li} and I_{La} are the integrated Li K and La $N_{2,3}$ intensities within an energy window of width ΔE starting close to the energy threshold of the ionization energy edges, and $\sigma_{\text{La}}(\alpha, \beta, \Delta E)$ and $\sigma_{\text{Li}}(\alpha, \beta, \Delta E)$ are the partial ionization cross

sections integrated over a collection semi-angle β and corrected from the incident beam convergence semi-angle α . Under chosen operating conditions, the collection semi-angle β was 16.7 mrad and the incident beam convergence semi-angle α was 13.7 mrad. The partial ionization cross sections $\sigma_{\text{La}}(\alpha, \beta, \Delta E)$ and $\sigma_{\text{Li}}(\alpha, \beta, \Delta E)$ were calculated using a Hartree-Slater model with a relative error of 20%, finally giving the ratio value, $\text{Li/La} = 1.19$. This was in excellent agreement with the ratio value derived from refined XRD analyses, $\text{Li/La} = 1.14$. The analysis of local elemental distributions of the constituents in individual garnet grains, including

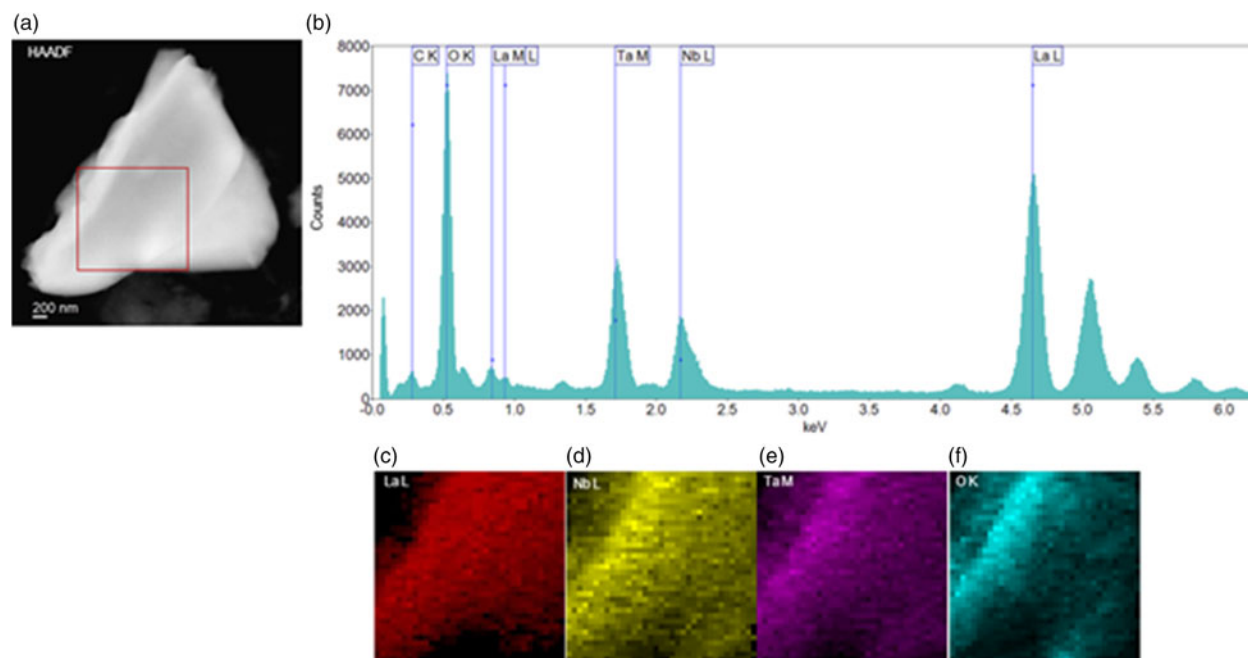


Figure 11. STEM-windowless EDX SI of a grain fragment of the L1000 garnet powder. (a) HAADF STEM image of an individual powder grain. (b) Sum X-ray spectrum acquired in the area marked by the red box. (c), (d), (e) and (f) Lanthanum La L (red), niobium Nb L (yellow), tantalum Ta M (magenta), and oxygen O K (turquoise) X-ray maps acquired over the marked area. The peaks at about 0.6, 1.3, and 4.2 keV are minor characteristic X-ray peaks of lanthanum, the La M_{21} at 0.638 keV and the La $L_{\alpha 1}$ at 4.126 keV, and tantalum, the Ta M_{21} at 1.328 keV.

lanthanum, niobium, tantalum, and oxygen, was completed using STEM-windowless EDX SI, as shown in Figure 11. The results indicated mesoscale-to-nanoscale inhomogeneities at the level of individual grains induced under thermochemical and mechanical processing, particularly by adding Li_2CO_3 to compensate for lithium losses during sintering. So, aggregated particles containing oxygen, but not lanthanum, niobium, and tantalum which were assigned to Li_2CO_3 often formed non-uniform shells surrounding garnet grains. Aggregated particles containing oxygen, but not lanthanum, niobium, and tantalum [see Figures 8(f)–8(i)] were assigned to Li_2CO_3 that often formed nonuniform shells surrounding garnet grains. At different stages of the multistep fabrication process, thermochemical and mechanical processing conditions could essentially influence surface structures, intergrain contacts, local electronic structure, and transport properties of the garnet ceramics.

C. Ionic conductivity

In general, our EIS measurements revealed two-time constant ionic conductivity behavior, reflecting the contributions from both the bulk grains and grain boundaries of the garnet samples. Typical Nyquist plots (imaginary vs. real impedance) measured at 25 °C for samples L750 and L1000 are shown in Figure 12. An equivalent circuit consisting of $(RQ)_b(RQ)_{gb}$ [inset of Figure 12(a)] is used to fit the experimental data, where R and Q represent the resistance and constant phase element, respectively, for both the bulk grain and the grain boundary. These Nyquist plots are similar to those of $\text{Li}_5\text{La}_3\text{M}_2\text{O}_{12}$ ($M = \text{Nb}, \text{Ta}$) (Thangadurai et al., 2003), showing bulk resistance at the higher frequency region (left side of the plot) and some grain boundary contributions at the lower frequency region. Moreover, the Nyquist plot of

L750 and L1000 measured at 85 °C [Figure 12(b)] showed a small tail at the lower frequency region as the result of mobile ion blockage in the electrolyte/electrode interfaces (Mariappan et al., 2013). This data was fit to the equivalent circuit $(RQ)_b(RQ)_{gb}Q_{el}$, with the interfacial constant phase element (Q_{el}) added in series. The magnitude of capacitance of the bulk crystal and grain boundary regions was calculated from the constant phase element using the relation, Eq. (3).

$$C = Q_o(\omega'_m)^{n-1} \quad (3)$$

where Q_o is the constant phase element, ω'_m is the characteristic angular frequency (rad s^{-1}) at which the imaginary part of the impedance ($-Z''$) has the maximum value, and n is a numeric parameter obtained from the fitting of the Nyquist plot (Hsu and Mansfeld, 2001). For L1000, at 25 °C, the characteristic frequency (defined as $f_c = (2\pi RC)^{-1}$) in the bulk crystal and grain boundary regions was 5276.82 and 0.22 Hz, respectively. Similarly, for L750, at the same temperature, the value of the characteristic frequency in the bulk crystal and grain boundary regions was 1189.89 and 1.42 Hz, respectively. The average bulk capacitance was found to have a value of 40 pF/cm², while the average grain boundary capacitance had an average value of 40 nF/cm². The larger capacitance gives rise to the relatively low characteristic frequency of the grain boundary response. Neither capacitance value varied systematically with measurement temperature nor sample processing temperature.

The total conductivity of the pellets was calculated using the formula, Eq. (4).

$$\sigma_{\text{total}} = t/(R_{\text{total}}A) \quad (4)$$

where R_{total} is the sum of the bulk resistance and grain boundary resistance (Kotobuki and Kiyoshi, 2013) obtained from

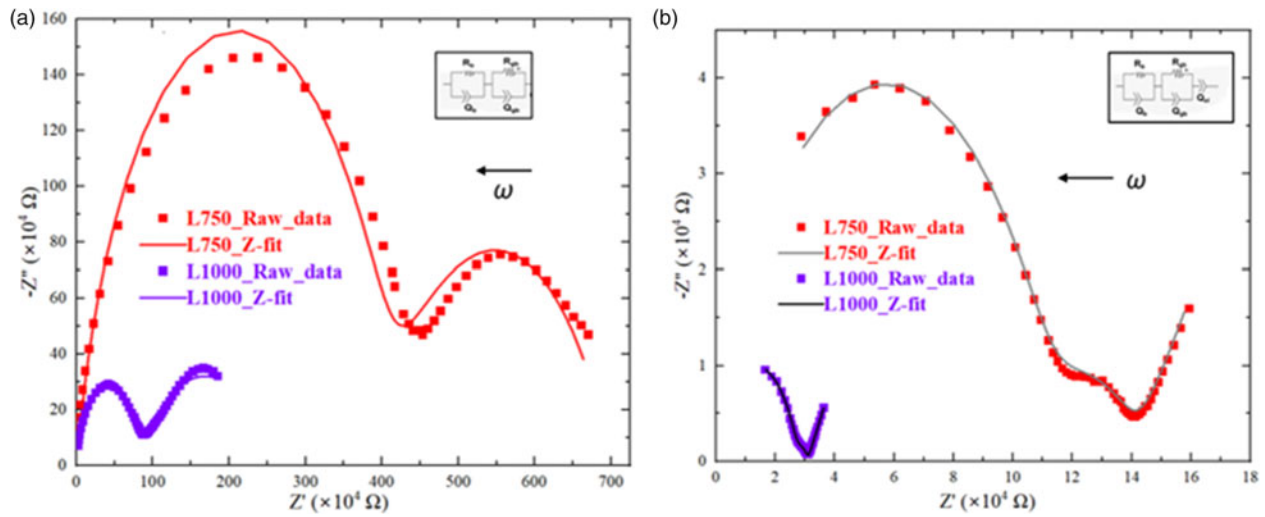


Figure 12. Nyquist plots obtained from EIS measurement. (a) Nyquist plots (25 °C) of $\text{Li}_{5-x}\text{La}_3\text{NbTaO}_{12-y}$ sintered at 750 °C (L750) and 1000 °C (L1000), with an inset showing schematic for equivalent circuit model $((R_b Q_b)(R_{gb} Q_{gb}))$; R is the resistance, Q is the constant phase element, subscript, b = bulk and gb = grain boundary and (b) nyquist plots (85 °C) of $\text{Li}_{5-x}\text{La}_3\text{NbTaO}_{12-y}$ sintered at 750 °C (L750) and 1000 °C (L1000), with an inset showing schematic for equivalent circuit model $((R_b Q_b)(R_{gb} Q_{gb}) Q_{el})$; R is the resistance, Q is the constant phase element, subscript, b = bulk, gb = grain boundary, and el = electrolyte/electrode interfaces.).

the analysis of the impedance plots, and t and A are the thickness and cross-sectional area of the pellet, respectively. Figure 13 represents the plot of σ_{total} (total conductivity in S cm^{-1} at 25 °C) vs. processing temperature. The total conductivities of L750 and L1000 at 25 °C, obtained from ac impedance data, are 1.71×10^{-8} and $7.12 \times 10^{-8} \text{ S cm}^{-1}$ within an 8.5% uncertainty and 11.6% uncertainty, respectively. Similarly, for L800, L850, L900, and L950, the total ionic conductivities at 25 °C were calculated to be $6.15 \times$

10^{-9} , 1.92×10^{-9} , 1.34×10^{-8} , and $4.78 \times 10^{-8} \text{ S cm}^{-1}$, respectively. From XRD results, the low values of the total conductivities for L750, L850, and L950 were due to a combined result of low Li content and the presence of impurity phases.

We used the brick layer model (BLM) to estimate the specific conductivity of both the grain and the grain boundary regions. Although the measured values of R_g and R_{gb} are of the same order, the volume they occupy in the sample is

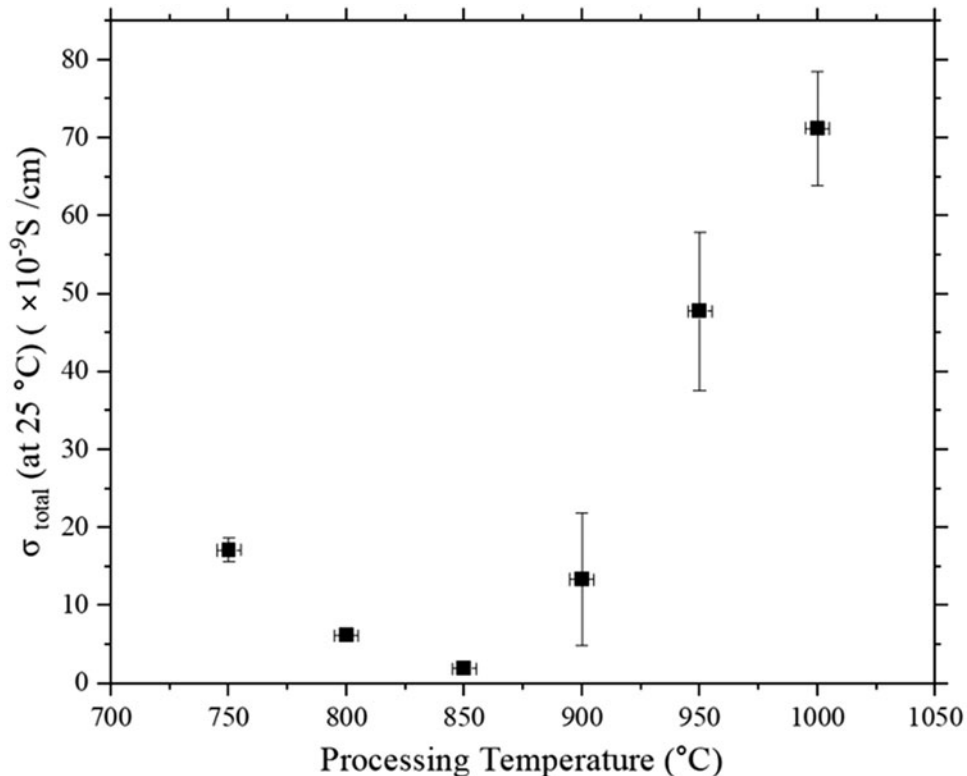


Figure 13. Total conductivity (σ_{total}) (S cm^{-1}) $\text{Li}_{5-x}\text{La}_3\text{NbTaO}_{12-y}$ at 25 °C vs. processing temperature (°C).

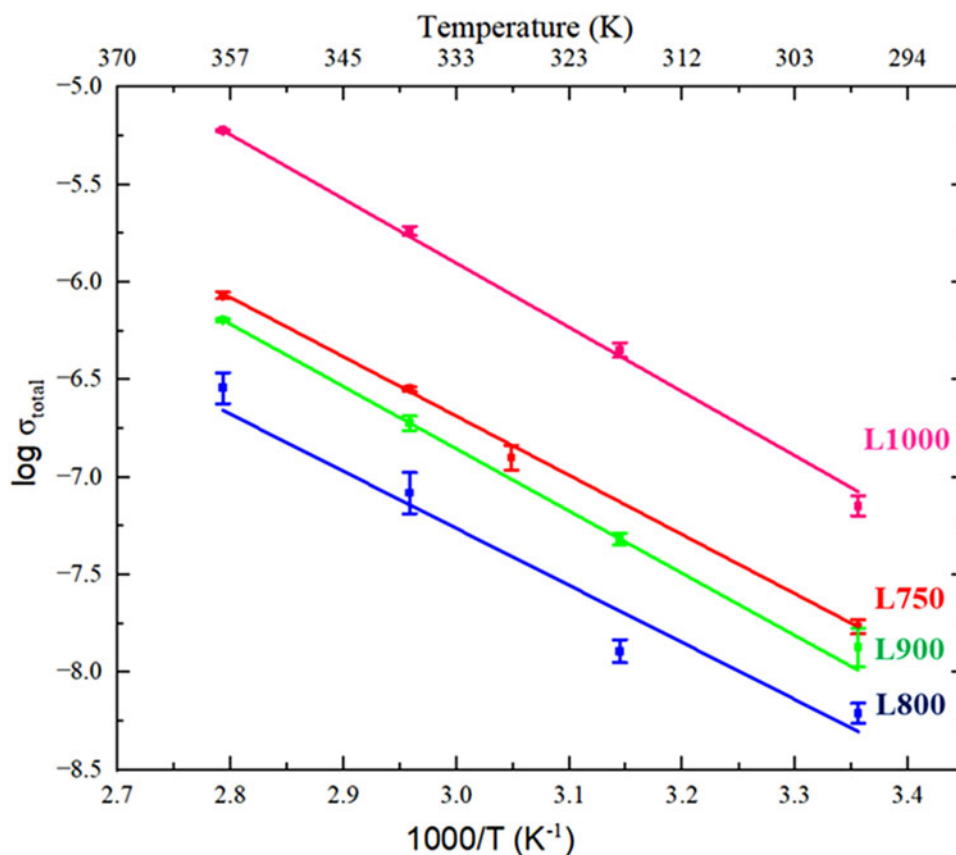


Figure 14. Arrhenius plots ($\log \sigma_{\text{total}}$ vs. $1000/T$), the box with the error bar represents the data point and regular line for linear fitting, for $\text{Li}_{5-x}\text{La}_3\text{NbTaO}_{12-y}$ sintered at different temperatures (L750, L800, L900, L1000).

significantly different. In the BLM (Mariappan et al., 2013), it is assumed that the permittivities of grains and grain boundaries are identical and that the relevant length scales can be estimated from the capacitance measured from each region, such that $C_g/C_{gb} = d/D$, where d is the thickness of the grain boundary, and D is the grain diameter (Mariappan et al., 2013). With this assumption, the specific conductivity of the grain can be expressed as $\sigma_g = t/(R_g A)$, while that of the grain boundary is given by $\sigma_{gb} = (1/R_{gb})(t/A)(C_b/C_{gb})$. Based on the average capacitance values, we obtain an average $C_b/C_{gb} = d/D = 0.001$, which results in an average $\sigma_b = 6.05 \times 10^{-7}$ and $\sigma_{gb} = 9.72 \times 10^{-9} \text{ S cm}^{-1}$ for the L1000 sample at 45 °C. The two orders of magnitude difference between σ_b and σ_{gb} are consistent with reports in the literature, e.g., see Mariappan et al. (2013).

The temperature dependence of the conductivity is expressed by the Arrhenius equation:

$$\sigma = A \exp(-E_a/k_B T) \quad (5)$$

where A is the pre-exponential factor, T is the absolute temperature, E_a is the activation energy, and k_B is the Boltzmann constant (Hummel, 2011). Figure 14 shows the Arrhenius plots. ($\log \sigma_{\text{total}}$ vs. $1000/T$) for total ionic conductivity for the samples L750, L800, L900, and L1000. The activation energies obtained in the temperature range of 25–85 °C vary from 0.59 ± 0.02 to 0.67 ± 0.02 eV for these samples. This range is somewhat higher than that of both end members $\text{Li}_5\text{La}_3\text{Nb}_2\text{O}_{12}$ (0.43 eV) and $\text{Li}_5\text{La}_3\text{Ta}_2\text{O}_{12}$ (0.56 eV) (Thangadurai et al., 2003). The sample L1000 had the highest

ionic conductivity among the members of the $\text{Li}_{5-x}\text{La}_3(\text{Nb,Ta})\text{O}_{12-y}$ solid solution series, most likely due to better crystallinity, compositional uniformity, and high Li content, as confirmed by analytical FESEM and S/TEM-EELS-EDX. However, this value is still lower than that of the solid solution end member $\text{Li}_5\text{La}_3\text{Ta}_2\text{O}_{12}$ ($1.3 \times 10^{-6} \text{ S cm}^{-1}$ (Weppner et al., 2006)), mainly due to the Li deficiency. Future work includes improvement of the synthesis procedure of retaining the Li content in the samples.

IV. SUMMARY

A master batch of the prospective garnet-based ceramic electrolyte for all solid-state lithium ion batteries with the nominal composition $\text{Li}_{5-x}\text{La}_3(\text{Nb,Ta})\text{O}_{12-y}$ was prepared using Li_2CO_3 , pre-heated La_2O_3 , Nb_2O_5 , and Ta_2O_5 , with conventional solid-state technique at 750 °C. Subsequent samples taken from the master batch were individually heat-treated at 750 °C (L750), 800 °C (L800), 850 °C (L850), 900 °C (L900), 950 °C (L950), and 1000 °C (L1000). X-ray Rietveld refinements corroborated the structure to be cubic $la-3d$ and that all samples are Li-deficient. At lower heat-treatment temperatures, the Nb/Ta ratio was found to be nominally 1:1, but at higher temperatures, Ta evaporated slightly. We also found that in sample L1000, the Li site (Li3) occupied a partially filled (96h) position, resulting in a greater number of sites for Li migration.

FESEM examination of the powders showed rough surface microtopography, complex morphologies, and partially coalescing crystallites. The grain shapes ranged from 4 to

15 μm in diameter and becoming more regular with sintering, displaying faceting and size growth and demonstrating higher ionic conductivity due to the larger grain size. Multisignal FESEM/EDX and probe-corrected STEM/EDX/EELS analyses confirmed the purity and expected compositions of the examined garnet ceramic powders indicating local inhomogeneities that usually occurred at the level of individual grains being induced by thermochemical and mechanical processing and the presence of lithium carbonate to compensate lithium losses during sintering. The atomic ratio Li/La for the L1000 sample was estimated as 1.19, in excellent agreement with the value from XRD, Li/La = 1.14. The X-ray powder diffraction reference pattern of L1000 has been submitted to the Powder Diffraction File (PDF).

Impedance spectroscopy revealed ionic conductivity behavior, in general, with two-time constants indicating contributions from both bulk and grain boundaries. The lowest ionic for L850 was assigned to lithium loss and the presence of impurities. The sample L1000 had the highest ionic conductivity due to better crystallinity, high Li content, and compositional uniformity, as confirmed by XRD, analytical FESEM, and S/TEM analyses.

ACKNOWLEDGMENT

ICDD is gratefully acknowledged for the Grants-in-Aid assistance, Grant# 0903.

REFERENCES

- Bachman, J. C., S. Muy, A. Grimaud, H. H. Chang, N. Pour, S. F. Lux, O. Paschos, F. Maglia, S. Lupart, P. Lamp, L. Giordana, and Y. Shao-Horn. 2016. "Inorganic Solid-State Electrolytes for Lithium Batteries: Mechanisms and Properties Governing Ion Conduction." *American Chemical Society, Chemical Reviews* 116 (1): 140–62. doi:10.1021/acs.chemrev.5b00563.
- Baral, A. K., S. Narayanan, F. Ramezanipour, and V. Thangadurai. 2014. "Evaluation of Fundamental Transport Properties of Li-Excess Garnet-Type $\text{Li}_{5+2x}\text{La}_3\text{Ta}_{2-x}\text{Y}_x\text{O}_{12}$ ($x = 0.25, 0.5$ and 0.75) Electrolytes Using AC Impedance and Dielectric Spectroscopy." *Physical Chemistry Chemical Physics* 16 (23): 11356–66. doi:10.1039/c4cp00418c.
- Cussen, E. J. 2006. "The Structure of Lithium Garnets: Cation Disorder and Clustering in a New Family of Fast Li^+ Conductors." *Chemical Communications* 4: 412–13. doi:10.1039/b514640b.
- Cussen, E. J., T. W. S. Yip, G. Oneill, and M. P. Ocallaghan. 2011. "A Comparison of the Transport Properties of Lithium-Stuffed Garnets and the Conventional Phases $\text{Li}_3\text{Ln}_3\text{Te}_2\text{O}_{12}$." *Journal of Solid State Chemistry* 184 (2): 470–75. doi:10.1016/j.jssc.2010.12.021.
- Dhivya, L., and R. Murugan. 2014. "Effect of Simultaneous Substitution of Y and Ta on the Stabilization of Cubic Phase, Microstructure, and Li^+ Conductivity of $\text{Li}_7\text{La}_3\text{Zr}_2\text{O}_{12}$ Lithium Garnet." *ACS Applied Materials and Interfaces* 6 (20): 17606–15. doi:10.1021/cm060992t.
- Drouin, D., A. R. Couture, D. Joly, X. Tastet, V. Aimez, and R. Gauvin. 2007. "CASINO V2.42 - A Fast and Easy-to-Use Modeling Tool for Scanning Electron Microscopy and Microanalysis Users." *Scanning* 29 (3): 92–101. doi:10.1002/sca.20000.
- Egerton, R. F. 2011. *Electron Energy-Loss Spectroscopy in the Electron Microscope*, 270–77. New York: Springer.
- Gates-Rector, S., and T. Blanton. 2019. "The Powder Diffraction File: A Quality Materials Characterization Database." *Powder Diffraction* 34 (4): 352–60. doi:10.1017/S0885715619000812.
- Geiger, C. A., E. Alekseev, B. Lasic, M. Fisch, T. Armbruster, R. Langner, M. Fechtelkord, N. Kim, T. Pettko, and W. Weppner. 2011. "Crystal Chemistry and Stability of " $\text{Li}_7\text{La}_3\text{Zr}_2\text{O}_{12}$ " Garnet: A Fast Lithium-Ion Conductor." *Inorganic Chemistry* 50 (3): 1089–97. doi:10.1021/ic101914e.
- Goodenough, J. B., and K. S. Park. 2013. "The Li-Ion Rechargeable Battery: A Perspective." *Journal of the American Chemical Society* 135 (4): 1167–76. doi:10.1021/ja3091438.
- Hsu, C. H., and F. Mansfeld. 2001. "Technical Note: Concerning the Conversion of the Constant Phase Element Parameter Y_0 into a Capacitance." *Corrosion Science Section Corrosion* 57 (9): 747–48.
- Hummel, R. E. 2011. "Electrical Properties of Polymers, Ceramics, Dielectrics, and Amorphous Materials." In *Electronic Properties of Materials*, 4th ed. 181–211. New York: Springer.
- Hyooma, H., and K. Hayashi. 1988. "Crystal Structure of $\text{La}_3\text{Li}_5\text{M}_2\text{O}_{12}$ ($M = \text{Nb}, \text{Ta}$)." *Materials Research Bulletin* 23 (10): 1399–407. doi:10.1016/0025-5408(88)90264-4.
- Kotobuki, M., and K. Kiyoshi. 2013. "Fabrication of All-Solid-State Battery Using $\text{Li}_5\text{La}_3\text{Ta}_2\text{O}_{12}$ Ceramic Electrolyte." *Ceramics International* 39 (6): 6481–87. doi:10.1016/j.ceramint.2013.01.079.
- Kotobuki, M., and M. Koishi. 2014. "Preparation of $\text{Li}_7\text{La}_3\text{Zr}_2\text{O}_{12}$ Solid Electrolyte via a Sol-Gel Method." *Ceramics International* 40 (3): 5043–47. doi:10.1016/j.ceramint.2013.09.009.
- Lazanas, A., and M. Prodromidis. 2022. "Electrochemical Impedance Spectroscopy - A Tutorial." *ACS Measurement Science Au* 3 (3): 162–93. doi:10.1021/acsmesuresciau.2c00070.
- Mariappan, C. R., K. I. Gnanasekar, V. Jayaraman, and T. Gnanasekaran. 2013. "Lithium Ion Conduction in $\text{Li}_5\text{La}_3\text{Ta}_2\text{O}_{12}$ and $\text{Li}_7\text{La}_3\text{Ta}_2\text{O}_{13}$ Garnet-Type Materials." *Journal of Electroceramics* 30 (4): 258–65. doi:10.1007/s10832-013-9792-1.
- Mauger, A., C. M. Julien, A. Paoletta, M. Armand, and K. Zaghib. 2019. "Building Better Batteries in the Solid State: A Review." *Materials* 12 (23): 3892–978. doi:10.3390/ma12233892.
- Mizuno, Y., H. Wagata, H. Onodera, K. Yubuta, T. Shishido, S. Oishi, and K. Teshima. 2013. "Environmentally Friendly Flux Growth of High-Quality, Idiomorphic $\text{Li}_5\text{La}_3\text{Nb}_2\text{O}_{12}$ Crystals." *Crystal Growth and Design* 13 (2): 479–84. doi:10.1021/cg3012348.
- Murugan, R., V. Thangadurai, J. Schwenzel, and W. Weppner. 2006. "Materials Development for High-Performance Lithium-Ion Batteries." *210th ECS Meeting, Abstract#195*.
- Narayanan, S., F. Ramezanipour, and V. Thangadurai. 2012. "Enhancing Li Ion Conducting of Garnet-Type $\text{Li}_5\text{La}_3\text{Nb}_2\text{O}_{12}$ by Y- and Li-Codoping: Synthesis, Structure, Chemical Stability, and Transport Properties." *Journal of Physical Chemistry C* 116 (38): 20154–62. doi:10.1021/jp304737x.
- Nemori, H., Y. Matsuda, M. Matsui, O. Yamamoto, Y. Takeda, and N. Imanishi. 2014. "Relationship Between Lithium Content and Ionic Conductivity in the $\text{Li}_{5+2x}\text{La}_3\text{Nb}_{2-x}\text{Sc}_x\text{O}_{12}$ System." *Solid State Ionics* 266 (15): 9–12. doi:10.1016/j.ssi.2014.08.001.
- O'Callaghan, M. P., D. R. Lynham, E. J. Cussen, and G. Z. Chen. 2006. "Structure and Ionic-Transport Properties of Lithium-Containing Garnets $\text{Li}_3\text{Ln}_3\text{Te}_2\text{O}_{12}$ ($\text{Ln} = \text{Y}, \text{Pr}, \text{Nd}, \text{Sm-Lu}$)." *Chemistry in Materials* 18 (19): 4681–89. doi:10.1021/cm060992t.
- Paoletta, A., W. Zhu, G. Bertoni, S. Savoie, Z. Feng, H. Demers, V. Gariepy, G. Girard, E. Rivard, N. Delaporte, A. Guerfi, H. Lorrman, C. George, and K. Zaghib. 2020. "Discovering the Influence of Lithium Loss on Garnet $\text{Li}_7\text{La}_3\text{Zr}_2\text{O}_{12}$ Electrolyte Phase Stability." *ACS Applied Energy Materials* 3 (4): 3415–24. doi:10.1021/acsaem.9b02401.
- Ramzy, A., and V. Thangadurai. 2010. "Tailor-Made Development of Fast Li-Ion Conducting Garnet-Like Solid Electrolytes." *ACS Applied Materials and Interfaces* 2 (2): 385–90. doi:10.1021/am900643t.
- Rietveld, H. M. 1969. "A Profile Refinement Method for Nuclear and Magnetic Structures." *Journal of Applied Crystallography* 2: 65–71. doi:10.1107/S0021889869006558.
- Thangadurai, V., H. Kaack, and W. Weppner. 2003. "Novel Fast Lithium Ion Conduction in Garnet-Type $\text{Li}_3\text{La}_3\text{M}_2\text{O}_{12}$ ($M = \text{Nb}, \text{Ta}$)." *Journal of the American Ceramic Society* 86 (3): 437–40. doi:10.1111/j.1151-2916.2003.tb03318.x.
- Thangadurai, V., S. Adams, and W. Weppner. 2004. "Crystal Structure Revision and Identification of Li^+ -Ion Migration Pathways in the Garnet-Like $\text{Li}_5\text{La}_3\text{M}_2\text{O}_{12}$ ($M = \text{Nb}, \text{Ta}$) Oxides." *Chemistry of Materials* 16 (16): 2998–3006. doi:10.1021/cm031176d.

- Thangadurai, V., S. Narayanan, and D. Pinzar. 2014. "Garnet-Type Solid-State Fast Li-Ion Conductors for Li Batteries: Critical Review." *Chemical Society Reviews* 43: 4714–27. doi:10.1039/c4cs00020j.
- Toby, H., and R. B. Von Dreele. 2013. "GSAS-II: The Genesis of a Modern Open-Source All Purpose Crystallography Software Package." *Journal of Applied Crystallography* 46 (2): 544–49. doi:10.1107/S0021889813003531.
- Weppner, W. J., R. Murugan, V. Thangadurai, and J. Schwenzel. 2006. "Materials Developments of High-Performance Lithium Ion Batteries." ECS Meeting Abstracts MA2006-02: 195. doi:10.1149/MA2006-02/4/195.
- Zheng, F., M. Kotobuki, S. Song, M. O. Lai, and L. Lu. 2018. "Review on Solid Electrolytes for All-Solid-State Lithium-Ion Batteries." *Journal of Power Sources* 389 (15): 198–213. doi:10.1016/j.jpowsour.2018.04.022.